Measuring Forces and Spatiotemporal Evolution of Thin Water Films between an Air Bubble and Solid Surfaces of Different Hydrophobicity

Chen Shi,[†] Xin Cui,[†] Lei Xie,[†] Qingxia Liu,[†] Derek Y. C. Chan,[‡,§] Jacob N. Israelachvili,[⊥] and Hongbo Zeng*[,†]

[†]Department of Chemical and Materials Engineering, University of Alberta, Edmonton, Alberta T6G 2 V4, Canada, [‡]Department of Mathematics and Statistics, University of Melbourne, Parkville 3010, Australia, [§]Department of Chemistry and Biotechnology, Swinburne University of Technology, Hawthorn 3122, Australia, and [⊥]Department of Chemical Engineering, Materials Department, University of California, Santa Barbara, California 93106, United States

ABSTRACT A combination of atomic force microscopy (AFM) and reflection interference contrast microscopy (RICM) was used to measure simultaneously the interaction force and the spatiotemporal evolution of the thin water film between a bubble in water and mica surfaces with varying degrees of hydrophobicity. Stable films, supported by the repulsive van der Waals—Casimir—Lifshitz force were always observed between air bubble and hydrophilic mica surfaces (water contact angle, $\theta_w < 5°$) whereas bubble attachment occurred on hydrophobized mica surfaces. A theoretical model, based on the Reynolds lubrication theory and the augmented Young—Laplace equation including the effects of disjoining pressure, provided excellent agreement with experiment results, indicating the essential physics involved in the interaction between air bubble and solid surfaces can be elucidated. A hydrophobic interaction free energy per unit area of the form: $W_H(h) = -\gamma(1 - \cos\theta_w)\exp(-h/D_H)$ can be used to quantify the attraction between bubble and hydrophobized solid substrate at separation, h, with γ being the surface tension of water. For surfaces with water contact angle in the range $45° < \theta_w < 90°$, the decay length D_H varied between 0.8 and 1.0 nm. This study quantified the hydrophobic interaction in asymmetric system between air bubble and hydrophobic surfaces, and provided a feasible method for synchronous measurements of the interaction forces with sub-nN resolution and the drainage dynamics of thin films down to nm thickness.

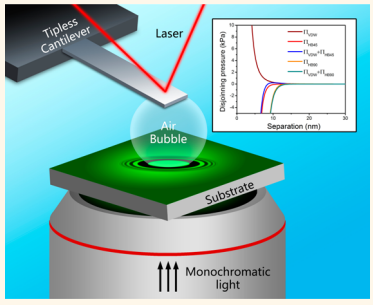

KEYWORDS: bubble · hydrodynamic force · hydrophobic interaction · AFM · mica · thin film drainage

Bubbles are an important component in a wide range of traditional industrial and engineering applications such as foam formation,[1] froth flotation[2] and microfluidic devices.[3] More recently bubbles are found to have important roles as an ultrasound imaging contrast agent,[4−6] in enhancing membrane permeability and molecular uptake,[7−9] as a stimuli-responsive carrier for drug and gene delivery,[4,10−13] as a water-driven micromotor,[14] as template for synthesis of micro- and nanoparticles[15,16] used in catalysis,[17] in heterogeneous cavitation[18] and in surface cleaning.[19] In many of these applications, the interactions between bubbles and solids of different hydrophobicity in aqueous environments such as electrostatic, hydrophobic, specific ligand—receptor interactions and hydrodynamic interaction are the critical determining factors for achieving desired characteristics and functionality of bubbles.[13,20−25] Because of the intrinsic hydrophobicity of bubbles, hydrophobic interaction is one of the most important nonspecific interactions that guides assembly and adsorption of hydrophobic or amphiphilic molecules and particles at the air/water interface.[21−23,26−28]

The hydrophobic interaction has been recognized for decades, yet its precise physical origin remains to be quantified, although different models have been proposed.[27,29−33] To date, quantitative force measurements of hydrophobic interactions were mainly conducted on solid surfaces using the surface force apparatus (SFA) and atomic force microscope (AFM).[31,32,34−40] An exponential dependence on separation with decay lengths of 0.3 nm to >1.0 nm has been reported for

* Address correspondence to hongbo.zeng@ualberta.ca.

Received for review November 19, 2014 and accepted December 16, 2014.

Published online December 16, 2014
10.1021/nn506601j

the hydrophobic interaction in different material systems[27,35,38] and the presence of nanobubbles on hydrophobic surfaces and dissolved gases have also been found to cause long-range attraction.[37,41−44] On the other hand, reports on hydrophobic interaction involving deformable bubbles or droplets were rather limited, most likely due to the complex coupling of forces and surface deformation during interaction.[30,45,46] In contrast to the strong elasticity-controlled deformation energetics of solid surfaces, weaker surface energy governs the deformation of the air/water interface of bubbles in response to external forces, such as velocity-dependent hydrodynamic force and separation-dependent colloidal forces.[21,47] Therefore, the drainage process of the thin liquid film confined between an air bubble and a solid surface can be more complex than that confined between two solid surfaces. To achieve a complete understanding of the interaction between air bubbles and solid surfaces, it is of critical importance to make synchronous measurements of interaction forces and visualization of the spatiotemporal evolution of the confined thin water film.

Recently, direct measurement of interaction force between an air bubble and solid surfaces has been successfully achieved using the AFM with the colloidal probe technique[46,47] and bubble probe technique.[48−50] Repulsive van der Waals forces were observed between an air bubble and hydrophilic surfaces (*e.g.*, mica) that stabilized a confined thin water film,[49,51] whereas an attractive hydrophobic attraction was found to be responsible for bubble attachment and immobilization on hydrophobic substrates.[48] In such AFM studies, absolute separation between the interacting surfaces and associated deformation can only be obtained indirectly through theoretical modeling. On the other hand, visualization of the film drainage process and spatial-temporal evolution of the trapped water film between an air bubble and hydrophilic glass without direct force measurements has been accomplished using optical interferometry and the results could be modeled quantitatively.[51−53] However, simultaneous measurements of the interaction force and spatial-temporal evolution of the confined thin liquid film associated with the dynamic interactions of deformable bubble and droplet have not been attempted to date.

In this work, we have integrated the capabilities of atomic force microscope (AFM) with reflection interference contrast microscopy (RICM) (Figure 1), and, for the first time, investigated the interaction between an air bubble and mica surfaces with varying degrees of surface hydrophobicity through synchronous measurements of the interaction force and spatial-temporal visualization of the thin film drainage process. The interaction forces were measured with the AFM by driving a cantilever-anchored air bubble toward the solid surface. The fringe patterns that arise from interference between light reflected from the air/water interface of the bubble and the mica/water interface were obtained with RICM and analyzed using an improved mathematical method reported recently.[54] This method enables the reconstruction of bubble−water surface profiles with nanometer-scale resolution.[54]

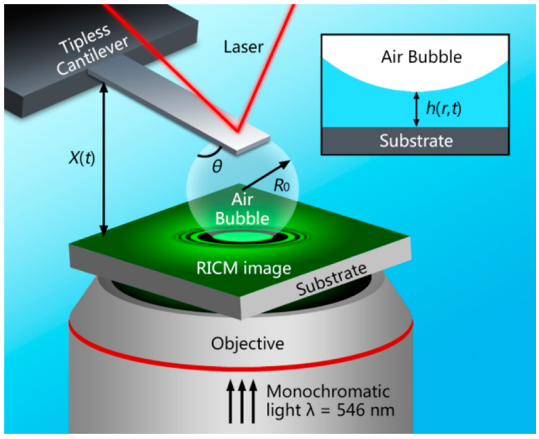

Figure 1. Experiment setup of using an AFM coupled with RICM for synchronous measurements of interaction forces and visualization of the spatiotemporal evolution of the confined thin liquid film between an air bubble of radius R_0 and a solid substrate. The air bubble is anchored on a tipless cantilever. The inset shows a schematic of the thin axisymmetric liquid film with thickness $h(r, t)$ between the air bubble and the substrate, where r is the radial coordinate.

A theoretical model has been applied to interpret the measured forces and predict the evolution of the thin water film profiles during the interaction that can be compared directly with experimental results.[48,49] The asymmetric hydrophobic interaction between an air bubble and a hydrophobized solid surface was also quantified for the first time based on the AFM-RICM measurements. More generally, this study demonstrates the feasibility of simultaneously probing interaction force profiles and thin film drainage dynamics involving deformable surfaces based on the AFM. The technique can be readily extended to study the interactions in systems involving deformable bubbles and droplets with the potential to provide guidance for designing bubble-loaded drug molecules and nanoparticles as well as to predict the assembly process of particles on bubble surfaces.

RESULTS AND DISCUSSION

A micrometer-size air bubble (radius R_0 = 60−100 μm) anchored on a custom-made AFM tipless rectangular cantilever (400 × 70 × 2 μm) was used to measure the interaction with mica surfaces with varying degrees of hydrophobicity (Figure 1). The air bubble was immobilized on a well-defined circular gold patch (diameter 65 μm, thickness 30 nm) at one end of the cantilever that was hydrophobized with a layer of self-assembled 1-dodecanethiol.[48,55] The position of the cantilever and hence the air bubble was accurately controlled by a piezo-electric transducer and variation of the actual displacement, $\Delta X(t)$ of the

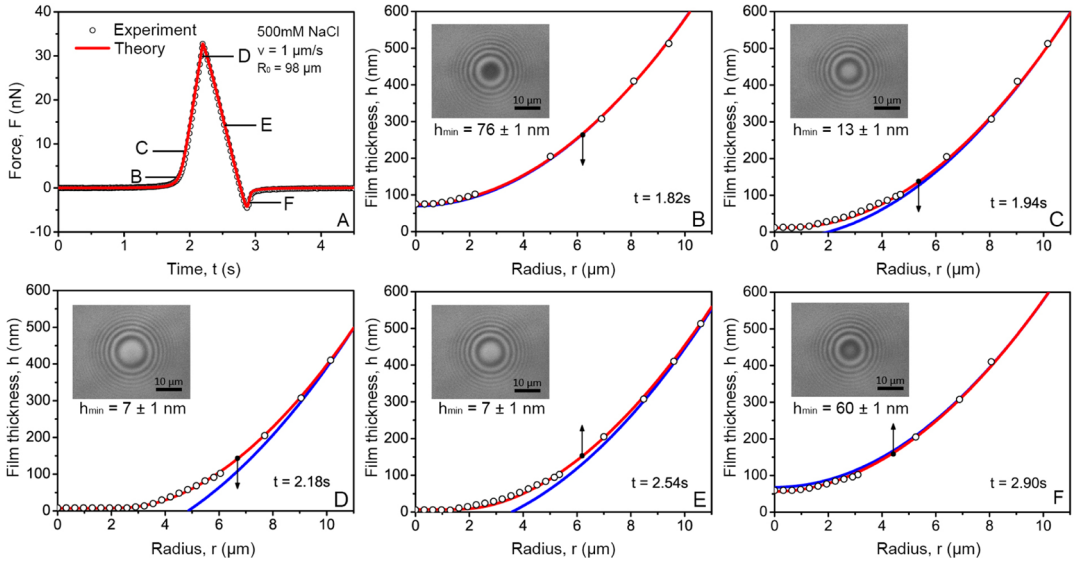

Figure 2. Time variations of the force and thin water film profile $h(r, t)$ during interaction between an air bubble and a hydrophilic mica surface in 500 mM NaCl solution. The bubble radius was 98 μm, and the nominal driving velocity of bubble was $v = 1$ μm/s. The open circular symbols are experimental results obtained from AFM-RICM measurements and the red solid lines are theoretical predictions. The blue solid lines are the spherical profile from outer part of the air bubble that corresponds to the profile of an undeformed bubble. The insets are interference fringe patterns from which the film profiles were deduced. The arrows indicate the driving direction of the air bubble, toward or away from the substrate. (A) Interaction force F as a function of time t; (B−F) confined film profile $h(r, t)$ at selected times indicated on the force curve in (A).

cantilever with time t, was measured and recorded with a linear variable differential transformer (LVDT) that is an integral part of the AFM.[56,57] The time-dependent interaction force was measured by monitoring the deflection of the cantilever with a known spring constant through changes in the position of a laser beam reflected from the cantilever on a photodiode detector. For a typical measurement, the air bubble was first driven toward ("approach") the mica surface until bubble attachment occurred or until a desired cantilever deflection was reached, whereupon it was then driven away ("retract") from the mica surface. The RICM interference patterns generated with monochromatic green light (wavelength 546.1 nm) were obtained with a Nikon Ti−U inverted microscope and were recorded with a video camera. The RICM images were processed with the *ImageJ* software (National Institutes of Health, USA) and the film thickness profiles were obtained by analysis of fringe order and light intensity of the interference patterns (see Supporting Information RICM image analysis).[54] The measurements were repeated at least 10 times at different positions on at least two surfaces with good reproducibility.

Bubble *vs* Hydrophilic Mica Surface. Before examining interactions between a bubble and mica surfaces with varying degrees of hydrophobicity, we first consider the simpler case of an unmodified hydrophilic mica surface for which all interaction forces are known.[48,49] This will help establish the experimental protocol and validate the theoretical model used to analyze subsequent experimental results. In Figure 2, we show the time variation of the measured force and the profile of the confined water film between an air bubble with radius of 98 μm and a freshly cleaved hydrophilic mica surface in 500 mM NaCl solution at a nominal velocity of $v = 1$ μm/s. At this high salt concentration, the electrical double layer (EDL) interaction between the bubble and the mica surface was highly screened so its contribution, $\Pi_{EDL}(h(r, t))$, to the overall disjoining pressure $\Pi(h(r, t))$ was negligible. The disjoining pressure due to van der Waals (VDW) interaction $\Pi_{VDW}(h(r, t))$, calculated using the full Lifshitz theory is repulsive at all separations (see van der Waals Interaction in Supporting Information).[58,59] Therefore, a thin water film is maintained between the air bubble and the hydrophilic mica surface, supported by the repulsive VDW interaction that prevents the air bubble from attaching to hydrophilic mica surface.

As shown in Figure 2, the time-dependent interaction force measured by AFM and profiles of the confined thin water film obtained from RICM measurements at different times (open circular symbols) agreed very well with theoretically predicted results (red solid lines). The RICM interference patterns are shown as insets in Figure 2B−F. The symmetry of the inference patterns confirms the assumption of axisymmetric geometry of the confined thin water film during interaction. The initial bubble-mica separation at the time datum $t = 0$ s, was calculated to be $h(r = 0, t = 0) = 3.08 \pm 0.01$ μm by fitting the force curve with theoretical model, the validity of that was verified with AFM coupled with confocal microscope in a previous report.[20] At time $t =$ 1.82 s (Figure 2B), the cantilever displacement $\Delta X(t)$ measured by the LVDT was 3.02 μm, still less than the initial separation and the profile results, showed that the air bubble remained nearly spherical and the

minimum separation, $h(r = 0, 1.82\ s)$ was about 76 nm. The measured actual $\Delta X(t)$ is larger than $v \times t = 1.82\ \mu m$ because the actual instantaneous velocity determined by LVDT $dX(t)/dt$ was slightly different from the nominal driving velocity due to the nonlinearity of piezoelectric transducer.[50,55] At a separation of 76 nm, the magnitude of VDW force was negligible compared to the hydrodynamic interaction that was repulsive during approach because the water confined between the air bubble and mica surface had to be displaced. At time $t = 1.94$ s (Figure 2C), $\Delta X(t) = 3.22\ \mu m$, so the air bubble would have made contact with the mica surface if it remained undeformed. However, the film profile shows there was still a finite separation of about 13 nm at $r = 0$ between air bubble and mica, as the bubble is deformed with a flattened central region that is evident on comparing the experimental data (open circles) and theoretical predictions (red solid line) to the undeformed spherical profile (blue solid line). Such deformation was mainly caused by hydrodynamic repulsion as the VDW interaction was negligible at $h \geq 13$ nm. As the bubble was driven even closer to mica, at time $t = 2.18$ s, when $\Delta X(t)$ has exceeded the initial separation $h(r = 0, t = 0)$ by 0.52 μm, the interaction force has reached maximum repulsion with a water film of minimum thickness of 7 nm, confined in a flatten region of about 3 μm in radial extent, as shown in Figure 2D. At this stage, no further thinning of the confined water film could be observed even when the cantilever was driven even closer. Therefore, the hydrodynamic interaction in this flattened region was negligible (since $dh/dt \sim 0$) and the thin water film was supported by the disjoining pressure due to the repulsive VDW interaction, calculated to be 1470 Pa at this separation and equal to the Laplace pressure of the air bubble. After the retraction was initiated, in contrast to the solid particle case in which the hydrodynamic force would become attractive immediately, the interaction repulsion force between the air bubble and the mica surface gradually decreased until a maximum hydrodynamic attraction was reached because water needed to be drawn back into the confined film (Figure 2A,E). As shown in Figure 2E, at time $t = 2.54$ s, the overall interaction force still remained repulsive during retraction and although the film thickness increased at the outer region of the air bubble due to the retraction, it remained almost unchanged ($\sim$7 nm) at the central flattened region while the radial extent of the central flattened region decreased form 3 to 2 μm. At time $t = 2.90$ s (Figure 2F), an attractive force was measured due to the hydrodynamic suction effect and the bubble showed a slight "pimple" shape, where its central region was closer to the mica surface as compared with the spherical undeformed shape (blue solid line).[48,50]

At higher velocities, significant bubble deformation and film thinning behavior accompanied by stronger attractive forces can be observed during the retraction process owing to the stronger hydrodynamic suction effect (see Supporting Information Figure S4). It is evident from the results in Figure 2 for the force and the confined film profiles that the VDW repulsion prevented the air bubble from attaching onto hydrophilic mica surface. The RICM experiment results clearly validated the theoretical model that is based on the Reynolds lubrication theory to describe the hydrodynamics of film drainage and the augmented Young−Laplace equation, with the inclusion of the VDW disjoining pressure to describe deformation of the bubble surface.

Bubble *vs* Hydrophobized Mica Surfaces. Freshly cleaved mica surfaces were hydrophobized with octadecyltrichlorosilane (OTS) by a vapor deposition process under vacuum, and different surface hydrophobicity was achieved by varying deposition duration. The hydrophobicity of the surfaces was characterized by the static water contact angle, θ_w, of sessile water drops on the surfaces. We designate mica surface with different degrees of hydrophobicity by "mica-OTS-45" ($\theta_w = 45°$) and by "mica-OTS-90" ($\theta_w = 90°$) respectively. Figure 3 shows the interaction between an air bubble of radius $R_0 = 75\ \mu m$ and the mica-OTS-45 surface and the interaction between an air bubble of radius $R_0 = 81\ \mu m$ and the mica-OTS-90 surface. As distinct from the results shown in Figure 2, jump-in behaviors (indicated by arrows in Figure 3A,D) where the interaction force drastically turned from positive (repulsive) to negative (attractive), were observed for both mica-OTS-45 and mica-OTS-90 surfaces when the bubble was driven at a low velocity of 1 μm/s toward the mica. The jump-in behaviors indicated bubble attachment onto the hydrophobized surfaces, which led to strong capillary bridging attraction due to formation of an air capillary bridge between the tipless cantilever and the solid surface. The attachment behaviors were also verified by the evolution of the interference patterns. For both cases, the air bubble could not be detached from the mica surface by retracting the cantilever because of the strong capillary adhesion between the bubble and hydrophobized surface. In fact, for the mica-OTS-90 case, the air bubble could even spontaneously detach from the cantilever during retraction, due to the stronger surface hydrophobicity than mica-OTS-45.

The hydrophobized mica-OTS-45 and mica-OTS-90 surfaces have a root-mean-square (rms) roughness of $\sim$0.3 nm as confirmed by AFM imaging. Since the coated OTS layer on the mica surface was very thin, $\sim$1 nm as reported previously, its effect on the VDW interaction could be neglected for separation larger than 2 nm.[21,60] As discussed above, the VDW interaction between mica surface and air bubble in water was repulsive at all separations and the EDL interaction was fully suppressed under the concentrated salt solution

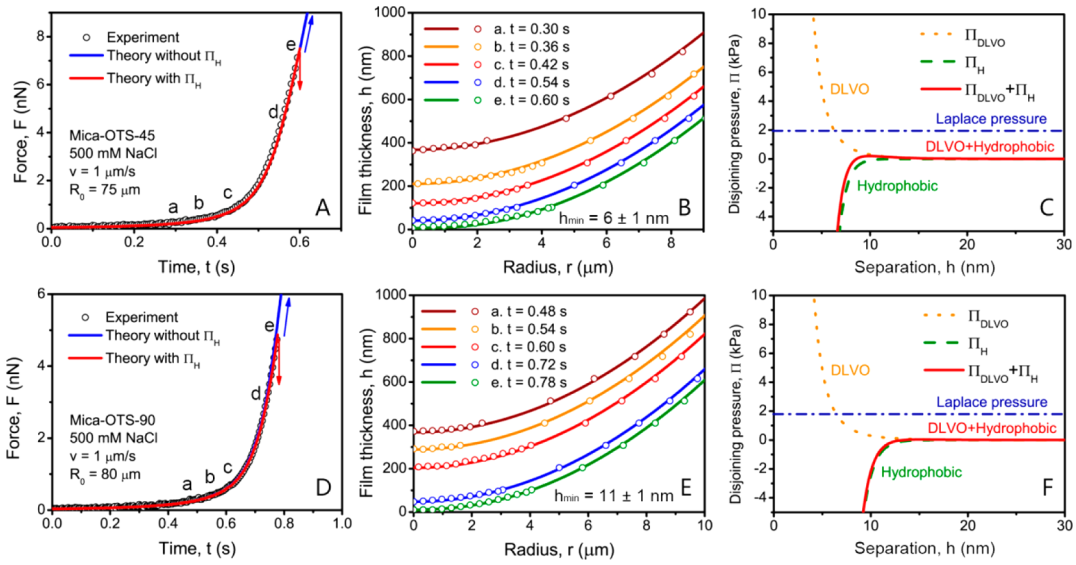

Figure 3. Interaction and disjoining pressure profiles between an air bubble and hydrophobized mica surfaces: mica-OTS-45 ($\theta_W = 45°$) (A−C) and mica-OTS-90 ($\theta_W = 90°$) (D−F), in 500 mM NaCl solution. The nominal driving velocity of bubble was $v = 1$ μm/s. In (A) and (D), the red solid lines are theoretical calculations that included the hydrophobic attractive disjoining pressure (see text) and the blue solid lines are predicted theoretical results without the attractive hydrophobic interaction. The open circular symbols are experimental results obtained from AFM and RICM measurements. (A,C) Interaction force F as a function of time. (B,E) Evolution of the thin confined water film profile $h(r, t)$. (D,F) Variations of components of the disjoining pressure with separation.

condition. Therefore, an additional attractive interaction must be responsible for triggering the air bubble attachment—we attribute this to the attractive hydrophobic interaction between the air bubble and the hydrophobized mica. We recognize that interfacial nanobubbles have been observed by AFM imaging on various hydrophobic substrates that could lead to long-ranged attraction between the hydrophobic surfaces.[42−44,61−66] However, in this work, the RICM image has a normal resolution of ∼1 nm and lateral resolution of ∼150 nm. Therefore, the presence of nanobubbles with lateral size >150 nm could be excluded by RICM analysis. Tapping mode AFM imaging of the hydrophobized mica surfaces in 500 mM NaCl (Figure S4) further confirms the absence of nanobubbles on the surfaces. Therefore, interfacial nanobubbles can be ruled out as the source for the observed attraction between an air bubble and hydrophobized mica surfaces in the present study.

Recently, a general interaction free energy per unit area: $W_H(h) = -2\gamma Hy \exp(-h/D_H)$ has been proposed to describe the hydrophobic or hydrophilic interaction between two identical planar surfaces at separation, h where D_H is a characteristic decay length, γ is the interfacial energy of the surfaces and Hy (the so-called Hydra number) is the fraction of the hydrophobic region on the surface that may also depend on solvent conditions.[27,35,38] The decay length D_H has been measured to be about 1 nm for solid hydrophobic surfaces, and a shorter decay length of ∼0.3 nm was also measured between hydrophobic oil droplets very recently.[30,45]

For the asymmetric interaction between a planar air−water interface and a hydrophobized mica surface, a similar exponential form for the interaction free energy per unit area: $W_H(h) = -C \exp(-h/D_H)$ can be posited. The constant C can be derived from thermodynamic considerations of the limit $h \rightarrow 0$ that creates a solid−air interface with surface energy γ_{SA} from an air−water interface with surface energy γ, and a solid−water interface with surface energy γ_{SW} to give: $C = \gamma + \gamma_{SW} - \gamma_{SA}$. This together with the Young−Duprè equation at the three phase contact line: $\gamma_{SA} = \gamma_{SW} + \gamma \cos\theta_w$ gives $C = \gamma(1 - \cos\theta_w)$ and results in the following expression for the hydrophobic disjoining pressure between a bubble and a hydrophobized surface.

$$\Pi_H(h) = -dW_H/dh = -[\gamma(1 - \cos\theta_w)/D_H]\exp(-h/D_H) \quad (1)$$

For mica-OTS-45 and mica-OTS-90 surfaces, the constant $C = \gamma(1 - \cos\theta_w)$ was determined to be 21 and 72 mN/m, respectively and the corresponding decay length D_H was found by fitting the force-time data at $v = 1.0$ μm/s shown in (Figure 3A, D) to be 0.8 ± 0.1 nm for the interaction with the mica-OTS-45 surface and to be 1.0 ± 0.1 nm for the mica-OTS-90 surface. This fitted hydrophobic disjoining pressure was then used to calculate the confined film profiles at different times. As can be seen in Figure 3B,E, such predicted film profiles agree very well with the experimental data based on the analysis of interference patterns from RICM (Supporting Information Figure S5). The critical film thickness before attachment, that is at the point of rupture of the confined water film, was calculated to be

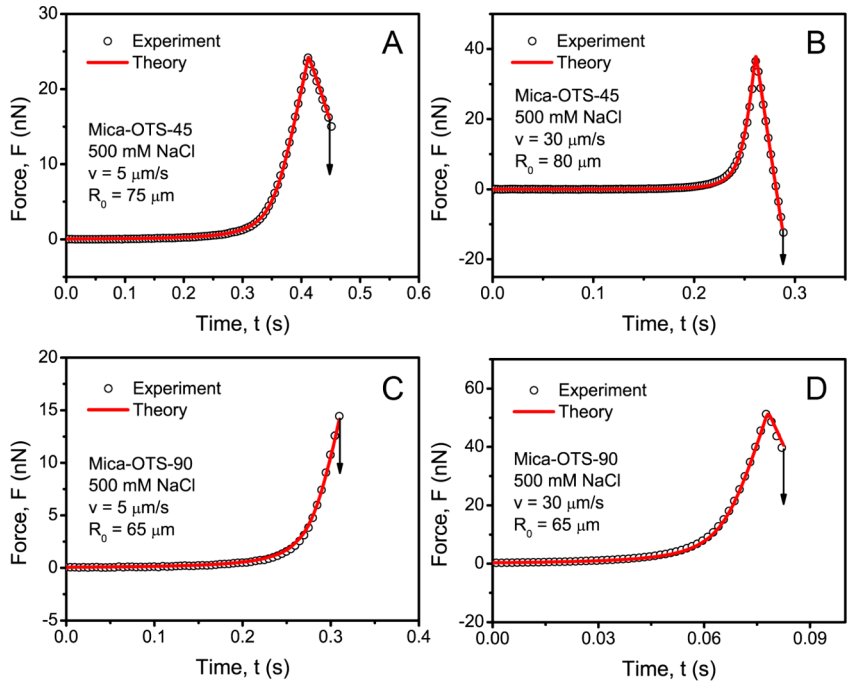

Figure 4. Interaction force between a bubble and hydrophobized mica surfaces: mica-OTS-45 ($\theta_w = 45°$) (A and B) and mica-OTS-90 ($\theta_w = 90°$) (C and D), in 500 mM NaCl solution with high velocities. The red solid lines are theoretical predictions. The open circular symbols are experiment force results obtained from AFM measurements. (A,C) Interaction at a nominal drive velocity of $v = 5$ μm/s. (B,D) Interaction at a nominal drive velocity of $v = 30$ μm/s.

~5.3 and ~9.5 nm for mica-OTS-45 case and mica-OTS-90 case, respectively, consistent with the experimental values of ~6 and ~11 nm measured by RICM. It is also worth noting that bubble attachment occurs at the critical separation where the magnitude of the negative disjoining pressure just exceeded the Laplace pressure of the bubble.

The same disjoining pressures for the bubble-hydrophobized mica interaction mica-OTS-45 and mica-OTS-90, without further adjustments, were used to calculate the force and the film profiles at other drive velocities. In Figure 4, we see that such predictions for the force for bubbles approaching mica-OTS-45 and mica-OTS-90 at nominal velocities in the range 5−30 μm/s agree very well with experimental data, and in particular, the model predicted the time of film rupture accurately. It is interesting to note that at these higher nominal drive velocities, water films remain stable on approach to the mica-OTS-45 surface because they are stabilized by higher repulsive hydrodynamic pressure. Film rupture only occurs during the retraction phase (Figure 4A,B) when the hydrodynamic pressure turns attractive and brings the bubble surface close enough to the hydrophobized mica surface to be within range of the attractive hydrophobic disjoining pressure $\Pi_H(h)$. On the other hand, for the mica-OTS-90 surface that has a stronger hydrophobic attraction film rupture occurs during approach at 5 μm/s, whereas a higher repulsive hydrodynamic repulsion at 30 μm/s is needed to prevent film rupture on approach, see Figure 4C,D.

In this work, the synchronous measurements of interaction forces and visualization of the spatiotemporal evolution of the confined thin water film between air bubble, that is inherently hydrophobic, and hydrohpobized mica surfaces demonstrate the significant role of hydrophobic interaction in this asymmetric system. The excellent agreement between theoretical predictions and experiment results based on AFM-RICM measurements indicates that $D_H = 0.8 \pm 0.1$ nm and $D_H = 1.0 \pm 0.1$ nm represent the characteristic decay length of hydrophobic interaction between the hydrophobic air bubble and hydrophobized mica-OTS-45 and mica-OTS-90, respectively.[21,29,31] The higher degree of surface hydrophobicity appears to increase the D_H value slightly. It is evident from our results that the characteristic decay length of hydrophobic interaction is influenced by the surface hydrophobicity that affects the structure and orientation of water molecules near the surface.[38,39] The asymmetric bubble-mica hydrophobic interaction free energy per unit area between the air bubble and the hydrophobic substrate can be described by

$$W_H(h) = -\gamma(1 - \cos\theta_w)\exp(-h/D_H) \qquad (2)$$

where γ is surface tension of water, θ_w is the static water contact angle on hydrophobic surface, h is the surface separation, D_H is the characteristic decay length that is system-dependent. On the basis of the analysis in this work, eq 2 is most likely applicable as a general potential function for hydrophobic interaction in asymmetric systems where deformable surfaces (*e.g.*, gas bubble, liquid droplet) are involved.

An attempt to represent the hydrophobic interaction free energy per unit area with a single power law of the form: $W_H(h) = -\gamma(1 - \cos\theta_w)[D_H/(h + D_H)]^n$ failed to provide agreement with experimental data at all drive velocities (see the Supporting Information for details).

A recent study on the interaction between two hydrophobic drops of fluorocarbon mixture with the same refractive index as water, in which the effects of VDW interaction was almost eliminated, demonstrated a short-ranged hydrophobic interaction with a characteristic decay length of 0.3 nm,[30,45] much shorter than that of hydrophobic interaction in solid/water/solid symmetric systems reported previously and the air bubble−water−solid asymmetric system in this work. It is interesting to note when θ_w =180°, eq 5 becomes $W_H(h) = -2\gamma \exp(-h/D_H)$, the same as the hydrophobic interaction free energy per unit area reported for the symmetric fluorocarbon/water/fluorocarbon system.

The difference between the observed decay lengths of ∼0.3 nm in soft oil/water/oil systems[30,45] and of 0.8−1.0 nm in air/water/solid in this work and elsewhere,[27] might be explained in terms of the difference in the ability of the hydrophobic substrate to respond as interfacial water molecules rearrange their position and orientation to compensate for the lost of hydrogen bonding. The mica surface that has been rendered hydrophobic by the deposition of a thin layer of OTS molecules is rigid, so the first few layers of adjacent water molecules have to restructure as a consequence of the loss of hydrogen bonding compared to water molecules in bulk. On the other hand, in the vicinity of the soft, fluid oil/water interface, both the water and oil molecules in their respective phases near the interface can adjust their structure to accommodate for the loss of hydrogen bonding in the aqueous phase and the change in the surface energetics in the oil phase. As a consequence, the disruption of the bulk water structure is expected to extend a shorter distance into the aqueous phase thereby giving rise to the observed shorter decay length, D_H in the hydrophobic interaction free energy per unit area in soft oil/water/oil systems. Indeed as two soft, deformable oil/water interfaces are brought together, it is expected that the interfacial structure in both the aqueous and the oil phase will change as a function of separation. However, precise quantification of such soft oil/water interfaces will require novel experimental studies and further theoretical modeling.

CONCLUSION

In this work, synchronous measurements of the interaction forces and the spatiotemporal evolution of the confined thin water film between air bubble and mica surfaces of different hydrophobicity were quantitatively achieved for the first time using an AFM coupled with RICM. The AFM-RICM experimental results are in complete accord with the theoretical model based on the Reynolds lubrication theory and the augmented Young−Laplace equation by including the effects of disjoining pressure. The excellent agreement between theory and experiments attests that the essential physics for the interaction between bubble and solid substrate has been elucidated. A hydrophobic interaction free energy per unit area of the form: $W_H(h) = -\gamma\ (1 - \cos\theta_w) \exp(-h/D_H)$, developed from thermodynamic considerations, is able to quantify the asymmetric interaction between an air bubble and hydrophobic mica substrates in predicting the attachment of the bubble at AFM drive speeds between 1−30 μm/s on OTS hydrophobized mica surfaces with water contact angle θ_w = 45° and 90°. The variation in the decay length, D_H observed for the hydrophobic interactions between bubble and rigid hydrophobized mica surfaces used here and between soft deformable oil/water interfaces[30,45] is attributed to the ability of interfacial molecules in the oil phase to accommodate changes in structure (position and orientation) of water molecules near the interface as a result of the loss of hydrogen bonding. The methodology for synchronous probing interaction force profiles and thin film drainage dynamics involving deformable surfaces can be extended to study the interaction mechanisms of a wide range of systems involving deformable bubbles and liquid droplets. Our results have the potential to provide insights into the basic understanding of the dynamic interaction mechanism between solid surfaces of different hydrophobicity in aqueous media and deformable bubbles/drops/emulsions to more general biological materials that would be useful for designing the loading of bubbles/drops with molecules and particles as targeted delivery systems as well as the assembly of designed structures at soft or hydrophobic interfaces.

EXPERIMENTAL METHODS

Experiment. A MPF-3D AFM (Asylum Research, Santa Barbara, CA) with a mounted Nikon Ti−U inverted microscope was used to investigate the interaction between air bubble and mica surfaces. A circular glass slide of an AFM fluid cell (radius of 35 mm) was mildly hydrophobized in 10 mM OTS in toluene solution for seconds to obtain a water contact angle of ∼50° to provide optimized hydrophobicity for immobilizing air bubble on the substrate. The air bubbles were carefully injected with a custom-made glass pipet with ultrasharp end. The immobilized air bubble was then picked up by a custom-made rectangular silicon AFM cantilever (400 × 70 × 2 μm), which had a strongly hydrohpobized circular gold patch at one end (diameter 65 μm, thickness 30 nm) for secure bubble anchoring.[48−50] Calibration

of the cantilever was done before bubble loading and the spring constant was determined to be 0.3−0.4 N/m using the Hutter and Bechhoefer method.[67] The air bubble was then moved over the mica surface for force measurements.

Mica surfaces were hydrophobized with octadecyltrichlorosilane (OTS) through a vapor deposition process. A freshly cleaved mica surface was placed in a vacuum desiccator with a small OTS reservoir for different durations to achieve different degrees of hydrophobicity, indicated by the water contact angle of sessile drops. Before use in AFM-RICM experiments, the hydrophobized mica surfaces were washed with large amounts of toluene, ethanol and Milli-Q water sequentially to remove physically adsorbed OTS molecules. The roughness of the hydrophobized mica surfaces was determined by AFM tapping mode imaging, showing very low rms roughness ~0.3 nm.

Theoretical Model. Since the velocities investigated in this work ranged from 1 to 30 μm/s, corresponding to very small Reynolds numbers $\sim 10^{-3}$ to 10^{-4}, which indicates the flow is in Stokes flow region, the Reynolds lubrication model[48,49] can be used for quantitative analysis of the thickness, $h(r, t)$ of the axisymmetric film drainage process

$$\frac{\partial h}{\partial t} = \frac{1}{12\mu r}\frac{\partial}{\partial r}\left(rh^3\frac{\partial p}{\partial r}\right) \tag{3}$$

Here μ is the viscosity of water, $p(r, t)$ is the excess hydrodynamic pressure relative to the bulk solution. Immobile boundary conditions at both air/water and solid/water interfaces were applied in contrast to classic fluid mechanics that suggested that the air/water interface should be fully mobile and could not sustain any shear stress. Recent work involving air bubble interaction indicated the applicability of the immobile boundary condition at the air/water interface. This could be due to a trace amount of surface active agents, including electrolyte, which can arrest boundary mobility while only lowering the surface tension by as little as 0.1 mN/m.

The augmented Young−Laplace equation

$$\frac{\gamma}{r}\frac{\partial}{\partial r}\left(r\frac{\partial h}{\partial r}\right) = \frac{2\gamma}{R_0} - p - \Pi \tag{4}$$

where R_0 is the radius of the bubble, $(2\gamma/R_0)$ is the Laplace pressure inside the air bubble, and Π is the disjoining pressure, was used to describe the deformation of air bubble during interaction. The contribution to the disjoining pressure Π comprised of the sum of the VDW interaction, calculated based on the full Lifshitz theory and the hydrophobic interaction was described in the main text.

The interaction force $F(t)$ is calculated by integrating $p(r,t)$ and $\Pi(h(r, t))$ based on Derjaguin approximation

$$F(t) = 2\pi\int_0^\infty [p(r, t) + \Pi(h(r, t))]r\, dr \tag{5}$$

More details of theoretical model are contained in the Supporting Information.

Conflict of Interest: The authors declare no competing financial interest.

Acknowledgment. This work was supported by the Natural Sciences and Engineering Research Council of Canada (NSERC), the Canada Foundation for Innovation (CFI), and the Alberta Advanced Education & Technology Small Equipment Grants Program (AET/SEGP) (H. Zeng). D.Y.C. Chan acknowledges support from the Australian Research Council. J.N. Israelachvili acknowledges support from the MRSEC Program of the National Science Foundation under Award DMR11-21053.

Supporting Information Available: Details of experimental, analysis and modeling protocols. This material is available free of charge *via* the Internet at http://pubs.acs.org.

REFERENCES AND NOTES

1. Durian, D. J.; Weitz, D. A.; Pine, D. J. Multiple Light-Scattering Probes of Foam Structure and Dynamics. *Science* **1991**, *252*, 686–688.
2. Ralston, J.; Fornasiero, D.; Hayes, R. Bubble-Particle Attachment and Detachment in Flotation. *Int. J. Miner. Process.* **1999**, *56*, 133–164.
3. Prakash, M.; Gershenfeld, N. Microfluidic Bubble Logic. *Science* **2007**, *315*, 832–835.
4. Stride, E.; Edirisinghe, M. Novel Microbubble Preparation Technologies. *Soft Matter* **2008**, *4*, 2350–2359.
5. Schutt, E. G.; Klein, D. H.; Mattrey, R. M.; Riess, J. G. Injectable Microbubbles as Contrast Agents for Diagnostic Ultrasound Imaging: The Key Role of Perfluorochemicals. *Angew. Chem., Int. Ed.* **2003**, *42*, 3218–3235.
6. Lindner, J. R. Microbubbles in Medical Imaging: Current Applications and Future Directions. *Nat. Rev. Drug Discovery* **2004**, *3*, 527–532.
7. Prentice, P.; Cuschierp, A.; Dholakia, K.; Prausnitz, M.; Campbell, P. Membrane Disruption by Optically Controlled Microbubble Cavitation. *Nat. Phys.* **2005**, *1*, 107–110.
8. Wrenn, S. P.; Dicker, S. M.; Small, E. F.; Dan, N. R.; Mleczko, M.; Schmitz, G.; Lewin, P. A. Bursting Bubbles and Bilayers. *Theranostics* **2012**, *2*, 1140–1159.
9. Chen, K.-J.; Chaung, E.-Y.; Wey, S.-P.; Lin, K.-J.; Cheng, F.; Lin, C.-C.; Liu, H.-L.; Tseng, H.-W.; Liu, C.-P.; Wei, M.-C.; Liu, C.-M.; Sung, H.-W. Hyperthermia-Mediated Local Drug Delivery by a Bubble-Generating Liposomal System for Tumor-Specific Chemotherapy. *ACS Nano* **2014**, *8*, 5105–5115.
10. Lentacker, I.; De Smedt, S. C.; Demeester, J.; Van Marck, V.; Bracke, M.; Sanders, N. N. Lipoplex-Loaded Microbubbles for Gene Delivery: A Trojan Horse Controlled by Ultrasound. *Adv. Funct. Mater.* **2007**, *17*, 1910–1916.
11. Lentacker, I.; De Smedt, S. C.; Sanders, N. N. Drug Loaded Microbubble Design for Ultrasound Triggered Delivery. *Soft Matter* **2009**, *5*, 2161–2170.
12. Mura, S.; Nicolas, J.; Couvreur, P. Stimuli-Responsive Nanocarriers for Drug Delivery. *Nat. Mater.* **2013**, *12*, 991–1003.
13. Cavalli, R.; Bisazza, A.; Lembo, D. Micro- and Nanobubbles: A Versatile Non-Viral Platform for Gene Delivery. *Int. J. Pharm.* **2013**, *456*, 437–445.
14. Soler, L.; Magdanz, V.; Fomin, V. M.; Sanchez, S.; Schmidt, O. G. Self-Propelled Micromotors for Cleaning Polluted Water. *ACS Nano* **2013**, *7*, 9611–9620.
15. Yec, C. C.; Zeng, H. C. Nanobubbles within a Microbubble: Synthesis and Self-Assembly of Hollow Manganese Silicate and Its Metal-Doped Derivatives. *ACS Nano* **2014**, *8*, 6407–6416.
16. Kovalenko, A.; Jouhannaud, J.; Polavarapu, P.; Krafft, M. P.; Waton, G.; Pourroy, G. Hollow Magnetic Microspheres Obtained by Nanoparticle Adsorption on Surfactant Stabilized Microbubbles. *Soft Matter* **2014**, *10*, 5147–5156.
17. Shen, G.; Zhang, X. H.; Ming, Y.; Zhang, L.; Zhang, Y.; Hu, J. Photocatalytic Induction of Nanobubbles on TiO_2 Surfaces. *J. Phys. Chem. C* **2008**, *112*, 4029–4032.
18. Belova, V.; Krasowska, M.; Wang, D.; Ralston, J.; Shchukin, D. G.; Moehwald, H. Influence of Adsorbed Gas at Liquid/Solid Interfaces on Heterogeneous Cavitation. *Chemical Science* **2013**, *4*, 248–256.
19. Liu, G.; Craig, V. S. J. Improved Cleaning of Hydrophilic Protein-Coated Surfaces Using the Combination of Nanobubbles and SDS. *ACS Appl. Mater. Interfaces* **2009**, *1*, 481–487.
20. Lozano, M. M.; Longo, M. L. Microbubbles Coated with Disaturated Lipids and DSPE-PEG2000: Phase Behavior, Collapse Transitions, and Permeability. *Langmuir* **2009**, *25*, 3705–3712.
21. Israelachvili, J. N. *Intermolecular and Surface Forces*, revised 3rd ed.; Academic Press: Waltham, MA, 2011.
22. Dickinson, E.; Ettelaie, R.; Kostakis, T.; Murray, B. S. Factors Controlling the Formation and Stability of Air Bubbles Stabilized by Partially Hydrophobic Silica Nanoparticles. *Langmuir* **2004**, *20*, 8517–8525.
23. Sanchez-Iglesias, A.; Grzelczak, M.; Altantzis, T.; Goris, B.; Perez-Juste, J.; Bals, S.; Van Tendeloo, G.; Donaldson, S. H., Jr.; Chmelka, B. F.; Israelachvili, J. N.; *et al.* Hydrophobic Interactions Modulate Self-Assembly of Nanoparticles. *ACS Nano* **2012**, *6*, 11059–11065.

24. Leckband, D. Measuring the Forces That Control Protein Interactions. *Annu. Rev. Biophys. Biomol. Struct.* **2000**, *29*, 1–26.
25. Tirrell, M.; Kokkoli, E.; Biesalski, M. The Role of Surface Science in Bioengineered Materials. *Surf. Sci.* **2002**, *500*, 61–83.
26. Allan, D. B.; Firester, D. M.; Allard, V. P.; Reich, D. H.; Stebe, K. J.; Leheny, R. L. Linear and Nonlinear Microrheology of Lysozyme Layers Forming at the Air-Water Interface. *Soft Matter* **2014**, *10*, 7051–7060.
27. Donaldson, S. H.; Røyne, A.; Kristiansen, K.; Rapp, M. V.; Das, S.; Gebbie, M. A.; Lee, D. W.; Stock, P.; Valtiner, M.; Israelachvili, J. Developing a General Interaction Potential for Hydrophobic and Hydrophilic Interactions. *Langmuir* **2014**, 10.1021/la502115g.
28. Lee, M. H.; Reich, D. H.; Stebe, K. J.; Leheny, R. L. Combined Passive and Active Microrheology Study of Protein-Layer Formation at an Air-Water Interface. *Langmuir* **2010**, *26*, 2650–2658.
29. Meyer, E. E.; Rosenberg, K. J.; Israelachvili, J. Recent Progress in Understanding Hydrophobic Interactions. *Proc. Natl. Acad. Sci. U. S. A.* **2006**, *103*, 15739–15746.
30. Tabor, R. F.; Grieser, F.; Dagastine, R. R.; Chan, D. Y. C. The Hydrophobic Force: Measurements and Methods. *Phys. Chem. Chem. Phys.* **2014**, *16*, 18065–18075.
31. Israelachvili, J.; Pashley, R. The Hydrophobic Interaction Is Long-Range, Decaying Exponentially with Distance. *Nature* **1982**, *300*, 341–342.
32. Mastropietro, D. J.; Ducker, W. A. Forces between Hydrophobic Solids in Concentrated Aqueous Salt Solution. *Phys. Rev. Lett.* **2012**, *108*, 106101:1−4.
33. Huang, D. M.; Chandler, D. Temperature and Length Scale Dependence of Hydrophobic Effects and Their Possible Implications for Protein Folding. *Proc. Natl. Acad. Sci. U. S. A.* **2000**, *97*, 8324–8327.
34. Pashley, R. M.; McGuiggan, P. M.; Ninham, B. W.; Evans, D. F. Attractive Forces between Uncharged Hydrophobic Surfaces—Direct Measurements in Aqueous-Solution. *Science* **1985**, *229*, 1088–1089.
35. Donaldson, S. H., Jr.; Lee, C. T., Jr.; Chmelka, B. F.; Israelachvili, J. N. General Hydrophobic Interaction Potential for Surfactant/Lipid Bilayers from Direct Force Measurements between Light-Modulated Bilayers. *Proc. Natl. Acad. Sci. U. S. A.* **2011**, *108*, 15699–15704.
36. Craig, V.; Ninham, B.; Pashley, R. Direct Measurement of Hydrophobic Forces: A Study of Dissolved Gas, Approach Rate, and Neutron Irradiation. *Langmuir* **1999**, *15*, 1562–1569.
37. Faghihnejad, A.; Zeng, H. Hydrophobic Interactions between Polymer Surfaces: Using Polystyrene as a Model System. *Soft Matter* **2012**, *8*, 2746–2759.
38. Donaldson, S. H., Jr.; Das, S.; Gebbie, M. A.; Rapp, M.; Jones, L. C.; Roiter, Y.; Koenig, P. H.; Gizaw, Y.; Israelachvili, J. N. Asymmetric Electrostatic and Hydrophobic-Hydrophilic Interaction Forces between Mica Surfaces and Silicone Polymer Thin Films. *ACS Nano* **2013**, *7*, 10094–10104.
39. Kristiansen, K.; Stock, P.; Baimpos, T.; Raman, S.; Harada, J. K.; Israelachvili, J. N.; Valtiner, M. Influence of Molecular Dipole Orientations on Long-Range Exponential Interaction Forces at Hydrophobic Contacts in Aqueous Solutions. *ACS Nano* **2014**, *8*, 10870–10877.
40. Perkin, S.; Kampf, N.; Klein, J. Long-Range Attraction between Charge-Mosaic Surfaces across Water. *Phys. Rev. Lett.* **2006**, *96*, 038301:1−4.
41. Faghihnejad, A.; Zeng, H. Interaction Mechanism between Hydrophobic and Hydrophilic Surfaces: Using Polystyrene and Mica as a Model System. *Langmuir* **2013**, *29*, 12443–12451.
42. Carambassis, A.; Jonker, L. C.; Attard, P.; Rutland, M. W. Forces Measured between Hydrophobic Surfaces Due to a Submicroscopic Bridging Bubble. *Phys. Rev. Lett.* **1998**, *80*, 5357–5360.
43. Thormann, E.; Simonsen, A. C.; Hansen, P. L.; Mouritsen, O. G. Force Trace Hysteresis and Temperature Dependence of Bridging Nanobubble Induced Forces between Hydrophobic Surfaces. *ACS Nano* **2008**, *2*, 1817–1824.
44. German, S. R.; Wu, X.; An, H.; Craig, V. S. J.; Mega, T. L.; Zhang, X. Interfacial Nanobubbles Are Leaky: Permeability of the Gas/Water Interface. *ACS Nano* **2014**, *8*, 6193–6201.
45. Tabor, R. F.; Wu, C.; Grieser, F.; Dagastine, R. R.; Chan, D. Y. C. Measurement of the Hydrophobic Force in a Soft Matter System. *J. Phys. Chem. Lett.* **2013**, *4*, 3872–3877.
46. Preuss, M.; Butt, H. J. Direct Measurement of Particle-Bubble Interactions in Aqueous Electrolyte: Dependence on Surfactant. *Langmuir* **1998**, *14*, 3164–3174.
47. Ducker, W. A.; Xu, Z. G.; Israelachvili, J. N. Measurements of Hydrophobic and DLVO Forces in Bubble-Surface Interactions in Aqueous-Solutions. *Langmuir* **1994**, *10*, 3279–3289.
48. Shi, C.; Chan, D. Y. C; Liu, Q.; Zeng, H. Probing Hydrophobic Interaction between Air Bubble and Partially Hydrophobic Surfaces Using Atomic Force Microscopy. *J. Phys. Chem. C* **2014**, *118*, 25000–25008.
49. Tabor, R. F.; Manica, R.; Chan, D. Y. C.; Grieser, F.; Dagastine, R. R. Repulsive van der Waals Forces in Soft Matter: Why Bubbles Do Not Stick to Walls. *Phys. Rev. Lett.* **2011**, *106*, 064501:1−4.
50. Vakarelski, I. U.; Manica, R.; Tang, X.; O'Shea, S. J.; Stevens, G. W.; Grieser, F.; Dagastine, R. R.; Chan, D. Y. C. Dynamic Interactions between Microbubbles in Water. *Proc. Natl. Acad. Sci. U. S. A.* **2010**, *107*, 11177–11182.
51. Manica, R.; Parkinson, L.; Ralston, J.; Chan, D. Y. C. Interpreting the Dynamic Interaction between a Very Small Rising Bubble and a Hydrophilic Titania Surface. *J. Phys. Chem. C* **2010**, *114*, 1942–1946.
52. Hendrix, M. H. W.; Manica, R.; Klaseboer, E.; Chan, D. Y. C.; Ohl, C.-D. Spatiotemporal Evolution of Thin Liquid Films During Impact of Water Bubbles on Glass on a Micrometer to Nanometer Scale. *Phys. Rev. Lett.* **2012**, *108*, 247803:1−4.
53. Parkinson, L.; Ralston, J. The Interaction between a Very Small Rising Bubble and a Hydrophilic Titania Surface. *J. Phys. Chem. C* **2010**, *114*, 2273–2281.
54. Contreras-Naranjo, J. C.; Ugaz, V. M. A Nanometre-Scale Resolution Interference-Based Probe of Interfacial Phenomena between Microscopic Objects and Surfaces. *Nat. Commun.* **2013**, *4*, 1919:1−9.
55. Tabor, R. F.; Grieser, F.; Dagastine, R. R.; Chan, D. Y. C. Measurement and Analysis of Forces in Bubble and Droplet Systems Using AFM. *J. Colloid Interface Sci.* **2012**, *371*, 1–14.
56. Dagastine, R. R.; Manica, R.; Carnie, S. L.; Chan, D. Y. C.; Stevens, G. W.; Grieser, F. Dynamic Forces between Two Deformable Oil Droplets in Water. *Science* **2006**, *313*, 210–213.
57. Manor, O.; Vakarelski, I. U.; Stevens, G. W.; Grieser, F.; Dagastine, R. R.; Chan, D. Y. C. Dynamic Forces between Bubbles and Surfaces and Hydrodynamic Boundary Conditions. *Langmuir* **2008**, *24*, 11533–11543.
58. Ninham, B. W. Parsegia.Va Vanderwaals Forces—Special Characteristics in Lipid-Water Systems and a General Method of Calculation Based on Lifshitz Theory. *Biophys. J.* **1970**, *10*, 646–663.
59. Dagastine, R. R.; Prieve, D. C.; White, L. R. The Dielectric Function for Water and Its Application to van der Waals Forces. *J. Colloid Interface Sci.* **2000**, *231*, 351–358.
60. Grabbe, A. Double-Layer Interactions between Silylated Silica Surfaces. *Langmuir* **1993**, *9*, 797–801.
61. Borkent, B. M.; Dammer, S. M.; Schoenherr, H.; Vancso, G. J.; Lohse, D. Superstability of Surface Nanobubbles. *Phys. Rev. Lett.* **2007**, *98*, 204502:1−4.
62. Walczyk, W.; Schoenherr, H. Closer Look at the Effect of AFM Imaging Conditions on the Apparent Dimensions of Surface Nanobubbles. *Langmuir* **2013**, *29*, 620–632.
63. Walczyk, W.; Schoen, P. M.; Schoenherr, H. The Effect of Peakforce Tapping Mode AFM Imaging on the Apparent Shape of Surface Nanobubbles. *J. Phys.: Condens. Matter* **2013**, *25*, 184005:1−11.
64. Zhang, X. H.; Zhang, X. D.; Lou, S. T.; Zhang, Z. X.; Sun, J. L.; Hu, J. Degassing and Temperature Effects on the Formation of Nanobubbles at the Mica/Water Interface. *Langmuir* **2004**, *20*, 3813–3815.

65. Walczyk, W.; Schoenherr, H. Characterization of the Interaction between AFM Tips and Surface Nanobubbles. *Langmuir* **2014**, *30*, 7112–7126.
66. Walczyk, W.; Hain, N.; Schoenherr, H. Hydrodynamic Effects of the Tip Movement on Surface Nanobubbles: A Combined Tapping Mode, Lift Mode and Force Volume Mode AFM Study. *Soft Matter* **2014**, *10*, 5945–5954.
67. Hutter, J. L.; Bechhoefer, J. Calibration of Atomic-Force Microscope Tips. *Rev. Sci. Instrum.* **1993**, *64*, 1868–1873.